AIAA JOURNAL
Vol. 33, No. 9, September 1995

Numerical Study of Hypersonic Leeward Flow over a Blunt Nosed Delta Wing

E. R. Mallett* and D. I. Pullin†
California Institute of Technology, Pasadena, California 91125
and
M. N. Macrossan‡
University of Queensland, Brisbane 4072, Queensland, Australia

A kinetic theory based Navier–Stokes solver has been implemented on a parallel supercomputer (Intel iPSC Touchstone Delta) to study the leeward flowfield of a blunt nosed delta wing at 30-deg incidence at hypersonic speeds. Computational results are presented for a series of grids for both inviscid and laminar viscous flows. Our present aim is to make a detailed comparison of the shock structure generated above the leeward surface for the inviscid and laminar viscous flows at Reynolds numbers of 2.25×10^5 and 2.25×10^6. In addition, comparisons are made between the present and other independent calculations of the same flows.

I. Introduction

THE design of reusable spacecraft such as the Hermes (currently under consideration by the European Space Agency) will be enhanced by an accurate computational prediction of the flowfield during hypersonic re-entry into the atmosphere. This is particularly important on the leeward side of lifting surfaces where vortex phenomena have been judged responsible for intense local heating.[1] The combined effects of the high spatial grid resolution necessary for accuracy, the complexity of model used, and the three dimensionality of the flow mean that these computations can only be performed in a reasonable amount of time by machines of the supercomputer class. In light of this, the present work was conducted on a parallel supercomputer, the Intel iPSC Touchstone Delta at the California Institute of Technology.

In the present paper we present calculations for the steady hypersonic flow about a blunt delta wing at incidence in a hypersonic gas flow at a freestream Mach number of 8.7. The body shape, the freestream conditions and the body temperature were chosen as those defined by problem 7 of the Workshop on Hypersonic Flows for Re-entry Problems held by the Institute National de Recherche en Informatique et en Automatique at Antibes, France in 1990 and 1991. This allows comparisons of the present results with those of other workers using different numerical methods and with the experimental measurements of Niezgodha et al.[2] Calculations are presented for both pseudoinviscid Euler flow and for laminar Navier–Stokes flow at Reynolds numbers based on body chord and freestream kinematic viscosity of $Re = 2.25 \times 10^5$ and $Re = 2.25 \times 10^6$ with the aim of making comparison of the detailed structure of the leeward flow produced by these cases.

In Sec. II we describe briefly the numerical method used (see the Appendix for further information) and give details of the boundary conditions used and the three different grids employed. Some aspects of the parallel code implementation are also discussed in Sec. II whereas the computed results are described in Sec. III. Comparisons with other calculations of the same flow and with experiment are discussed in Secs. IV and V. It is concluded that the general shock–vortex structure of the leeward flow resembles that found for leeward cone flow by Marconi[3] although the fine details differ owing to the difference of the blunt nose and the delta wing geometry.

Received April 15, 1994; revision received Feb. 17, 1995; accepted for publication Feb. 26, 1995.

*Research Fellow; currently Senior Engineer, Failure Analysis Associates, 149 Commonwealth Drive, Menlo Park, CA 94025. Member AIAA.
†Professor of Aeronautics, Graduate Aeronautical Laboratories.
‡Lecturer, Department of Mechanical Engineering.

II. Numerical Method

The equilibrium flux method (EFM) was first proposed by Pullin[4] and is an explicit finite volume technique for solving the inviscid Euler equations of compressible ideal gas flow. The strategy is to split the fluxes of the conserved quantities at the kinetic level as part of a scheme to solve the Boltzmann equation in moment form in the limit of small Knudsen number under the assumption that the local velocity distribution in cells is of a local Maxwellian form. Although in first-order form the EFM method is rather numerically diffusive,[5] incorporation of total variation diminishing (TVD) methodology produces a fast high-order method which has the properties of robustness and simplicity of implementation for the computation of multidimensional gas dynamic flows.[5] The scheme appears to be particularly well adapted to the computation of flows containing curved strong shocks and to the calculation of multispecies flows involving the interaction of either equilibrium or nonequilibrium species chemistry with gas dynamics.[6–8] EFM has been adapted to the solution of the Navier–Stokes equations (see Appendix) for a compressible gas by first making use of a monotone upstream centered schemes for conservation laws (MUSCL) slope limiting scheme to produce a high-order method.[9] Viscous corrections to the fluxes were then treated by decoupling the pseudoinviscid and the viscous components of the fluxes, computing the latter at a macroscopic level, and correcting the boundary conditions at a solid wall to enforce the no-slip condition. The hybrid method was tested by computation of the hypersonic laminar boundary layer on a flat plate, finding good agreement at high freestream Mach number with results obtained using a viscous Riemann solver applied to the same flow. A brief description of the EFM method is given in the Appendix.

The body considered for this work is a problem considered in the Hypersonic Flows for Re-entry Problems Workshop organized by INRIA. The particular problem is the calculation of flow past a blunt nosed delta wing of 70-deg sweep, flying at an angle of attack of 30 deg. The freestream Mach number is held fixed at $M_\infty = 8.7$, with a freestream temperature of 55 K. Laminar flow with $\gamma = 1.4$ is assumed chemically frozen and a fixed wall temperature of 300 K is employed. Reynolds numbers of 2.25×10^5 and 2.25×10^6 based on freestream conditions and body centerline chord and a Prandtl number of 0.72 are used for the viscous calculations.

The basic numerical grid is a CO type grid consisting of $36 \times 40 \times 72$ cells in the streamwise, radial, and azimuthal directions, respectively. Yaw is not considered so only one-half of the body is modeled due to symmetry. Two additional grids were created: the first is coarser than the original and was created by removal of every second grid point in each direction; the second is finer than the

original and was created using four-point Lagrange interpolation. We refer to the grids as grid 1 ($18 \times 20 \times 36$), grid 2 ($36 \times 40 \times 72$), and grid 3 ($72 \times 80 \times 144$).

The iPSC Delta is an experimental parallel machine developed at Intel. It is preceded by the Intel iPSC/2 based on the 80386 processor and by the iPSC/860 Gamma a product of the i860 chip. The Delta is an example of a multiple instruction stream/multiple data stream (MIMD) machine.[10] Primary memory is distributed equally amongst each of 512 computational nodes connected as a two-dimensional mesh. The overall theoretical maximum speed of the machine is 32 Gflops using all 512 computational nodes.

The parallel general purpose three-dimensional (PGP3D) code[11] was written in standard Fortran 77 and uses the communication calls of the Parasoft Express[12] operating system which allows portability between a number of parallel machines. In addition, the use of dummy libraries enables the code to be run on sequential type machines without modification. Only one version of the code needs to be maintained, with identical copies of this code being loaded into every processor at runtime.

Briefly, parallelization is achieved by distributing the physical domain of the grid amongst the available processors in such a way that the boundary surface area of each subgrid was minimized. This reduces the amount of communication between processors as compared to computation and, thus, the overhead associated with using this machine architecture. A series of ghost cells is used around the perimeter of each subgrid to implement boundary conditions.

III. Results

A. Grid Convergence

To compare the inviscid solutions obtained under identical freestream conditions on each of the grids, the property values at the arbitrary downstream station $x/L = 0.8$ are examined where L is the length of the wing from apex to trailing edge measured in the x–y plane of symmetry along the leeward surface. This station is illustrated in Fig. 1 for the medium resolution grid (grid 2). Figure 2 shows contours of density for each of the three grids at the given downstream station. From these contour plots it is apparent that for all grids a detached bow shock is captured. The position of this shock is approximately the same for each grid, but the largest grid clearly presents greater resolution of the shock because of the additional cells in the radial j direction, which is approximately normal to the shock. For each grid a large expansion occurs as the flow moves around the leading edge from the high-pressure windward side to the low-pressure leeward side of the wing, but the flow remains attached; no separation occurs. Because of the symmetry condition in the x–y plane the crossflow component of velocity of the inbound fluid on the leeward side must go to zero. Consequently, the fluid undergoes compression in the region between the plane of symmetry and a point approximately midway along the semispan. For the grid 3 calculation the compression appears as a shock attached to the surface of the wing at approximately the midway point. This shock can also be seen for the medium resolution grid (grid 2) but for the coarsest grid (grid 1) there are insufficient cells tangential to the leeward surface to resolve this shock. As a result the shock is smeared and appears more like a gradual compression. Farther away from the leeward surface, there is similarity between each of the solutions.

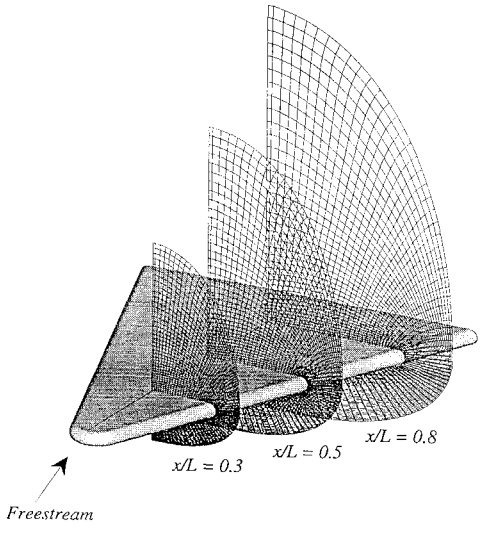

Fig. 1 Shape of blunt nosed delta wing and grid geometry at three stations.

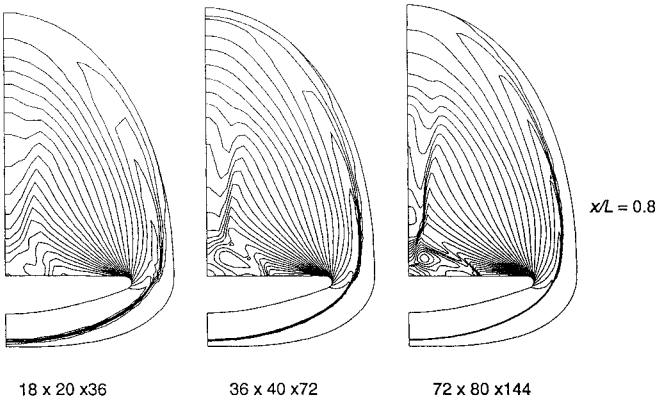

Fig. 2 Density contours for three grids at $x/L = 0.8$, inviscid flow.

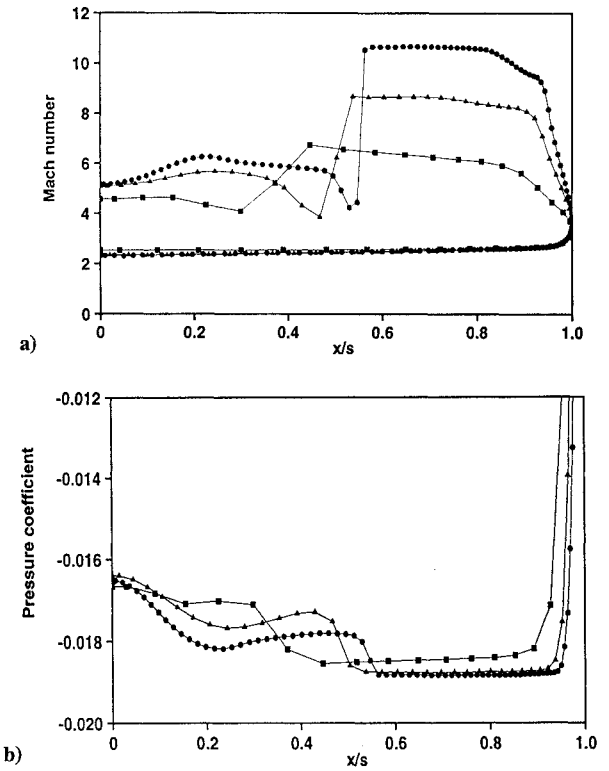

Fig. 3 Grid for $x/L = 0.8$, inviscid flow; ■ grid 1, ▲ grid 2, ● grid 3: a) Mach number variation along windward and leeward surfaces and b) pressure coefficient on leeward surface.

A quantitative comparison of the solutions can be made by considering the pressure coefficient and Mach number along the wing surface at the chosen downstream station. Figure 3 illustrates the variation of these two properties at the wing surface along the semispan. Note that owing to the difference in magnitude between the windward and leeward pressures only the leeward pressure is plotted. The comparison of Mach number on the windward side of the wing is good, particularly between the finer grids. This suggests the importance of grid resolution at the nose where surface curvature is high and the body cannot be considered conical. On the leeward surface the comparison is not as good, but there is clearly a trend toward the values shown for the finest grid. In each case smearing of

the crossflow shock is minimal and is captured in only two to three cells. An attempt was made at predicting the continuum solution using Richardson extrapolation of the results from the three grids. Unfortunately, this was unsuccessful because the limited amount of data (3 values per grid point) produced nonphysical results, such as negative density on the leeward surface. Thus, although decisive convergence was not achieved, the sharpness of the shock profiles together with a comparison with other numerical solutions for this flow (see Sec. IV) suggests effective convergence.

B. Inviscid Flow

Subsequent discussion will relate only to the results obtained for the finest grid (grid 3). Figure 4 shows contours of Mach number, log (P/P_∞), T/T_∞, and log (ρ/ρ_∞) where P, T, and ρ are the local pressure, temperature, and density on the leeward plane of symmetry. At the point of closest approach to the body, the bow shock is located midway between the nose surface and the forward

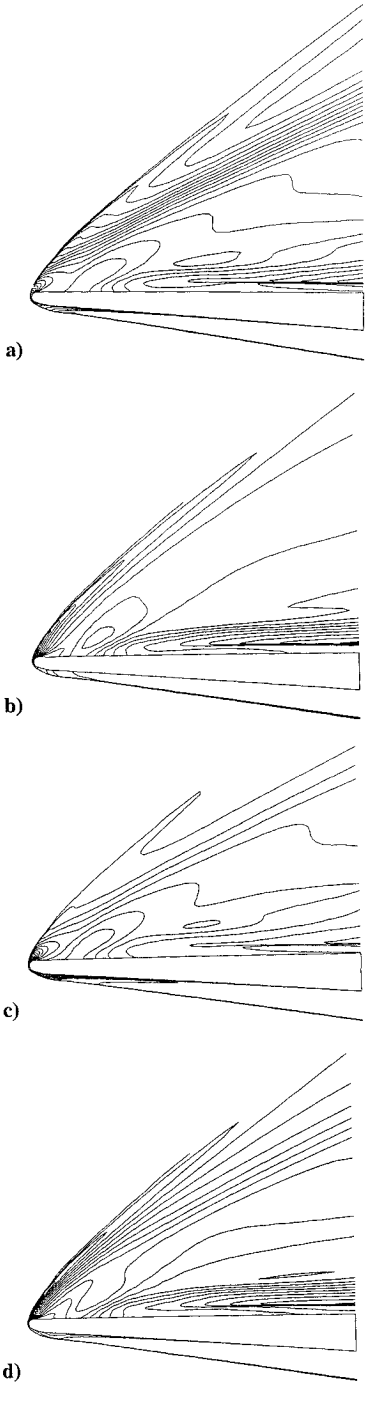

Fig. 4 Contours of invisid flow properties in the plane of symmetry: a) Mach number, b) log (P/P_∞), c) T/T_∞, and d) log (ρ/ρ_∞).

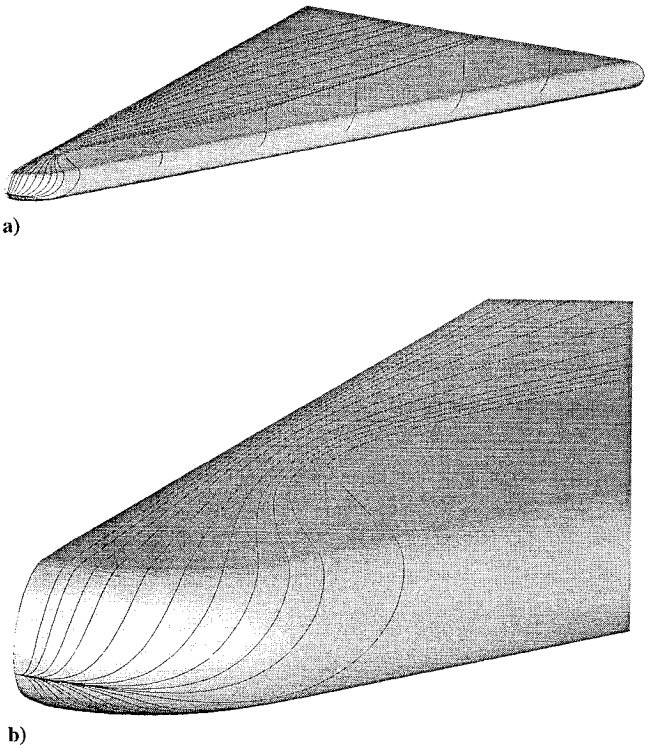

Fig. 5 Inviscid flow: a) surface streamlines near the nose and on the leeward surface and b) near-nose detail.

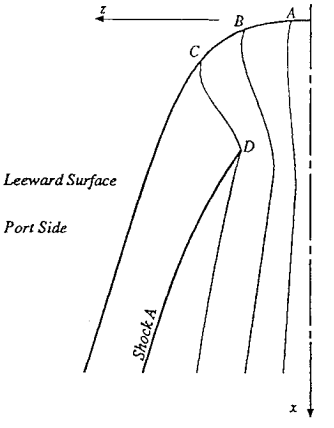

Fig. 6 Schematic of surface streamlines near nose, inviscid flow.

point of the grid, and so there are some 40 grid points between the shock and the surface. Of particular nose are the large Mach number gradients on the leeward side of the delta wing.

Figure 5 shows the surface streamlines on the leeward surface of the delta wing. In the stagnation region just on the underside of the nose, a bifurcation line is formed that distinguishes leeward and windward flow. A kinematic explanation of the leeward surface pattern of Fig. 5 is given in Fig. 6 which shows a schematic of surface streamlines on the leeward surface close to the nose. Close to the x–y plane of symmetry the crossflow velocity component of fluid flowing from the high-pressure underside of the wing is small, and the path of the fluid passing through point A is essentially in the downstream direction. Farther along the leading edge, the fluid passing through point B has a higher but still subsonic crossflow velocity. The symmetry condition causes the fluid to be turned in the downstream direction thus reducing the crossflow velocity. However, at some point farther along the leading edge (point C) the crossflow velocity of the fluid passing along this streamline becomes supersonic. To satisfy the symmetry condition the fluid is turned by means of an oblique shock wave that is produced at the surface of the wing. The vorticity produced by this shock causes the flow to separate from the surface of the wing and roll up into a vortex. The presence of this vortex causes fluid near the surface

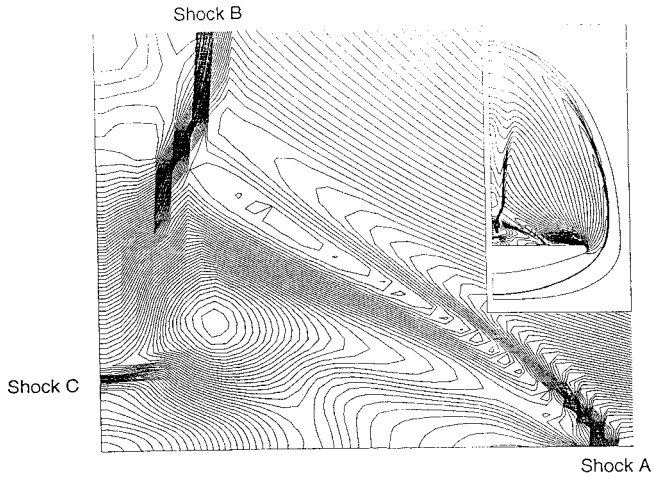

Fig. 7 Contours of log (ρ/ρ_∞) near leeward surface illustrating the presence of a pin-wheel shock, $x/L = 0.8$, inviscid flow.

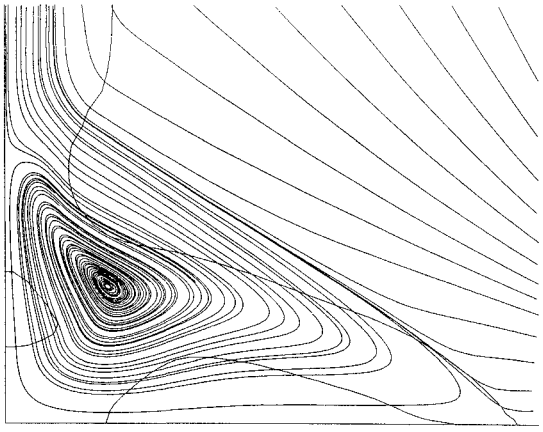

Fig. 8 Sectional streamlines and crossflow sonic lines on leeward surface near plane of symmetry, grid 3, $x/L = 0.8$, inviscid flow.

between the shock wave and the plane of symmetry to flow in an outboard direction.

In Fig. 7 we show a detail of the vortex/shock system density field at the downstream station $x/L = 0.8$ for grid 3 in the region between the surface shock and the x–y plane of symmetry. This figure shows the presence of two additional shocks inboard of the first. Figure 8 shows sectional streamlines[13] at the same location with crossflow sonic lines superimposed. The presence of the oblique shock at the surface of the wing (shock A) causes the flow to immediately separate as can be seen by the position of the separation streamline. Fluid on the outboard side of the separation is not entrained by the vortex but maintains a supersonic crossflow velocity component. Consequently, this fluid is turned away from the plane of symmetry by another oblique shock which sits approximately above the vortex core (shock B). This shock extends down through the separation streamline as fluid inboard of this streamline is accelerated to supersonic crossflow velocities by the action of the vortex. The fluid between the vortex core and the x–y plane of symmetry and below the critical point on the x–y plane is first accelerated. Because of the wing surface boundary condition the fluid is shocked (shock C) and then turned parallel to the surface in an outboard direction. This fluid then undergoes a series of expansions and compressions before being turned away from the surface in the direction of the separation streamline. The vortex/shock system is similar to that found by Marconi[3] for a circular cone under similar freestream conditions. The appearance of the shock system prompted Marconi to label such a system as a pinwheel shock.

Although the leading-edge radius is constant along the length of the wing, we would expect the flow to be largely conical downstream of the nose. To test this hypothesis, flow properties at the three downstream stations $x/L = 0.3$, $x/L = 0.5$, and $x/L = 0.8$ are examined for the finest grid. Figure 9 shows Mach number and the pressure coefficient at these downstream stations. It appears that on the windward surface and around the leading edge the flow is approximately conical. Inboard of the surface oblique crossflow shock there appears to be some disparity in the separated region yet the difference is within a few percent.

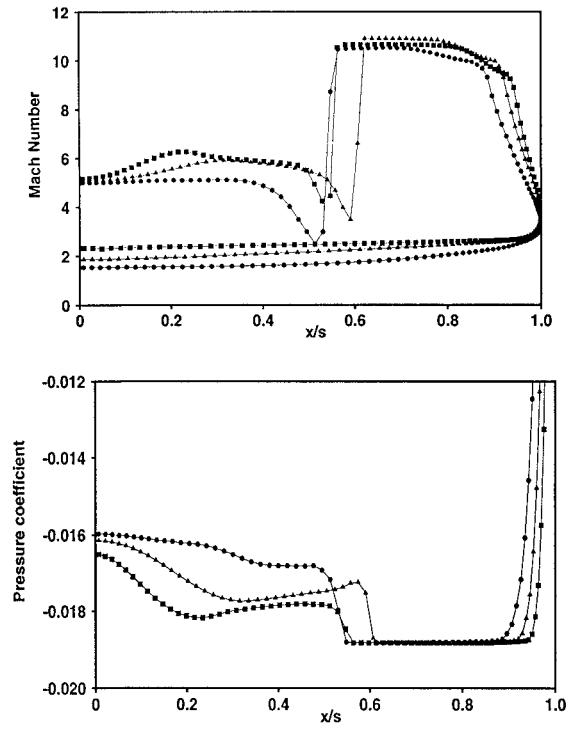

Fig. 9 Pressure coefficient and Mach number along the wing surface at three downstream stations, inviscid flow: ●, $x/L = 0.3$; ▲, $x/L = 0.5$; and ■, $x/L = 0.8$.

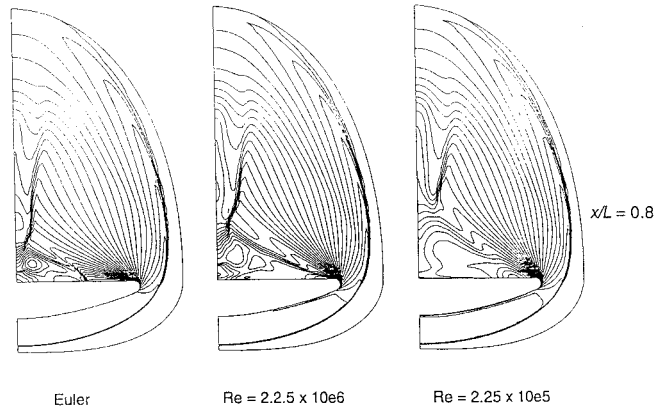

Fig. 10 Contours of log (ρ/ρ_∞) for inviscid and viscous flows, $x/L = 0.8$, Reynolds numbers as shown.

C. Comparison of Inviscid and Viscous Flows

To investigate the effects of viscosity on the flow two additional calculations were carried out using the finest grid at Reynolds numbers of 2.25×10^6 and 2.25×10^5. The freestream temperature was fixed at 55 K, a Prandtl number of 0.72 was used, and the wall temperature was fixed at 300 K. The variation of viscosity with temperature was assumed to follow the Sutherland law.

Figure 10 shows contours of density for the downstream station $x/L = 0.8$. It is evident that the bow shock is also well captured for the viscous cases and smearing is minimal. The strength and position of the bow shock is approximately the same for all three conditions, although the formation of a boundary layer on the windward surface changes the apparent surface geometry and displaces the shock position slightly farther outward from the wing.

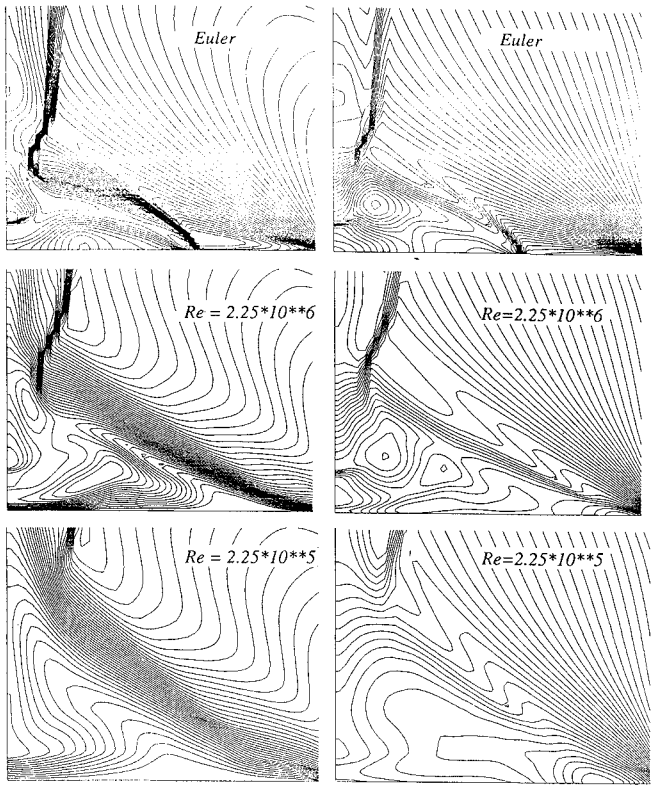

Fig. 11 Comparison of inviscid (Euler) and viscous flow fields in leeward flow region: Mach number (left) and log (ρ/ρ_∞) (right).

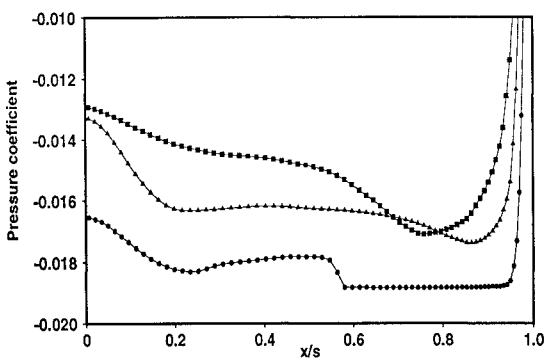

Fig. 12 Comparison of leeward surface pressure for inviscid and viscous cases: ●, inviscid; ▲, $Re = 2.25 \times 10^6$; and ■, $Re = 2.25 \times 10^5$.

We note that for grid 3, which has been stretched normal to the body surface, there were generally 15–20 points within the body boundary layer.

The major difference between the inviscid and viscous solutions occurs as the high-pressure fluid flows around the leading edge toward the leeward surface. For both viscous conditions the flow separates from the leeward surface just inboard of the leading edge, and there is no apparent cross flow shock. This can be more clearly seen in Fig. 11, which shows closer views of the separated regions. Away from this region the flows are similar. The leeward surface pressures in the separated regions for the viscous cases are less than that of the inviscid case as can be seen in Fig. 12. As a result slightly more lift is produced on the leeward surface. After separating, the characteristic vortex is formed in the separation region. Thus, leeward vortices are formed for both the inviscid and viscous flows but via quite different mechanisms: shock-induced separation for inviscid flow and three-dimensional boundary-layer separation for the viscous flows. For the larger Reynolds number condition the vortex is found to be slightly larger than for the inviscid case, and for the lower Reynolds number the vortex is larger again. The majority of lift is generated on the windward side of the wing, with a small part being generated by the suction pressure on the leeward surface. The lift on drag ratios were found to be similar for all three cases and are given in Table 1.

Table 1 Lift over drag ratios for Euler and viscous flows

Case	L/D ratio
Euler	1.340
$Re = 2.25 \times 10^5$	1.334
$Re = 2.25 \times 10^6$	1.312

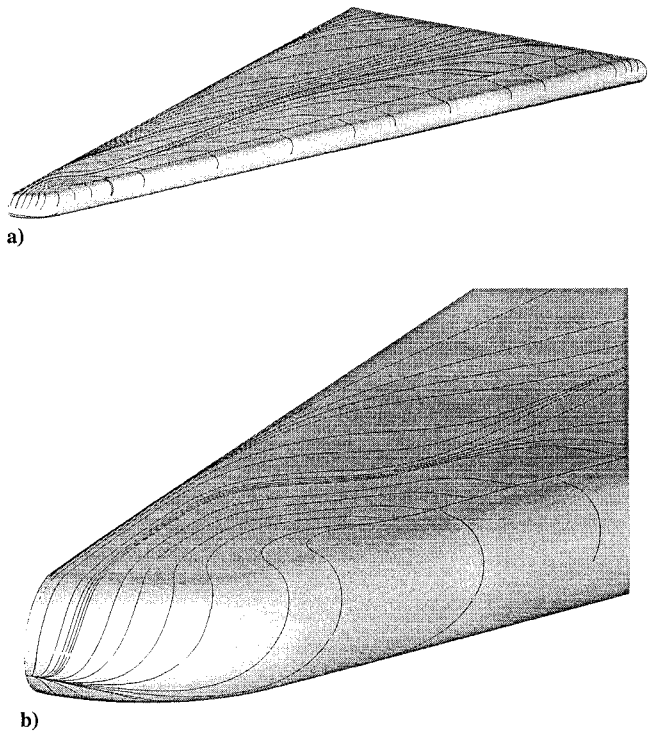

Fig. 13 Trajectories of the surface skin-friction field; $Re = 2.25 \times 10^6$: a) near the nose and on the leeward surface and b) near-nose detail.

Figure 13 shows skin friction lines on the leeward surface for a Reynolds number of 2.25×10^6. The stagnation region and the bifurcation streamline at the nose are in similar positions to that of the inviscid case. The separation line on the leeward surface can be clearly seen and is considerably closer to the leading edge than for inviscid flow. Because the majority of the fluid passing over the leeward surface is much colder than the surface, heat transfer is generally away from the body. However, in the region where the vortex is first formed (close to the nose) there is a region where the fluid temperature close to the wall is higher than the wall temperature resulting in heat transfer to the surface. This is a local effect and can be seen on the temperature contours in the plane of symmetry (not shown here) as a slight bump for a Reynolds number of 2.25×10^6 and as a bubble for 2.25×10^5.

IV. Comparison with Other Numerical Solutions

It is informative to compare the results obtained from this work with those presented by other researchers for the same body under identical freestream conditions. These results were originally presented at the Workshops on Hypersonic Flows for Re-entry Problems in Antibes, France, in 1990 and 1991. Contours of constant Mach number are compared at the downstream station $x/L = 0.8$. These are shown in Figs. 14 and 15. Le Toullec and Guillen[14] present results for inviscid flow obtained from the use of a space marching, MUSCL scheme. A multiblock grid was used with $39 \times 48 \times 48$ cells in the nose region and a second grid of $99 \times 48 \times 93$ cells was used for the remainder of the body. The nose portion was solved in a time marching manner, and the remainder was solved by space marching downstream one plane at a time. The method is implicit

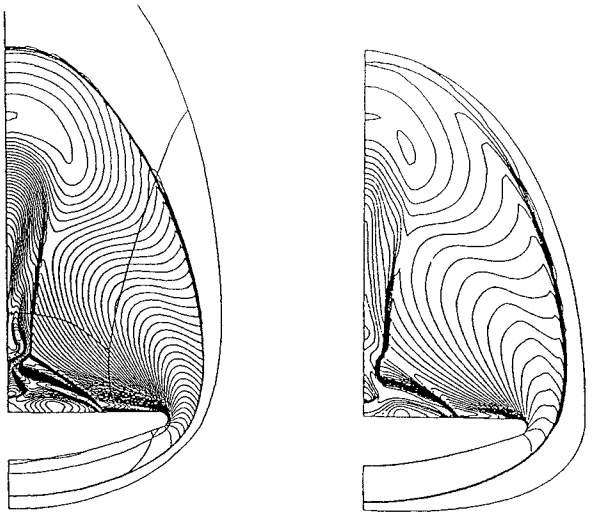

Fig. 14 Mach number contours, $x/L = 0.8$, inviscid flow: Le Toullec and Guillen[14] (left) and present calculation (right).

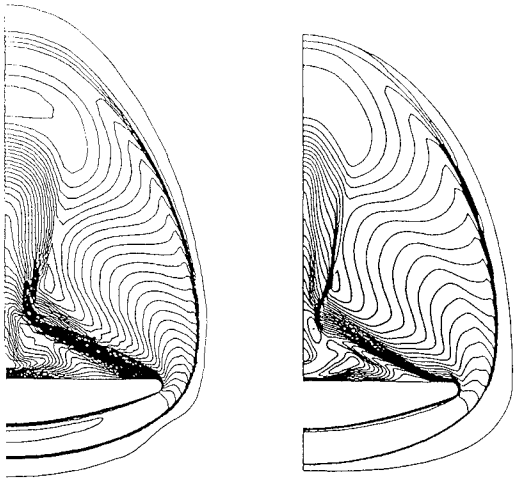

Fig. 15 Mach number contours, $x/L = 0.8$, $Re = 2.25 \times 10^6$: Menne[15] (left) and present calculation (right).

and so converges fairly quickly; in all only 60 iterations were required for an initial computation. The results from this computation were used to statically adapt the grid to the solution, and the computation was repeated. As there was thought to be insufficient resolution of the vortex region, a third calculation was carried out on a refinement of this region only, using the results form the previous calculation as boundary conditions. Figure 14 compares Mach number distributions at $x/L = 0.8$ from Ref. 14 with these from the present calculations. It is evident that the adaptive gridding gives better flow structure resolution in the shock/vortex region. However, the overall nature and location of the resolved flow features show good agreement with the present results, supporting our earlier assertion that we have obtained effective convergence with our finest grid.

A sample of a solution obtained for a viscous case is also considered. The freestream parameters are the same as used in the present work with $Re = 2.25 \times 10^6$. Again, Mach number contours are compared at the downstream station $x/L = 0.8$ and are shown in Fig. 14. Menne[15] uses a finite volume shock-capturing method based on Roe's approximate Riemann solver. The method is implicit and second order in space and viscous terms are obtained using centered differences. The code is used in a space marching mode on a grid of $63 \times 55 \times 53$ cells in the downstream, radial and azimuthal directions, respectively. Again, a comparison with the present work, shown in Fig. 15, gives good agreement

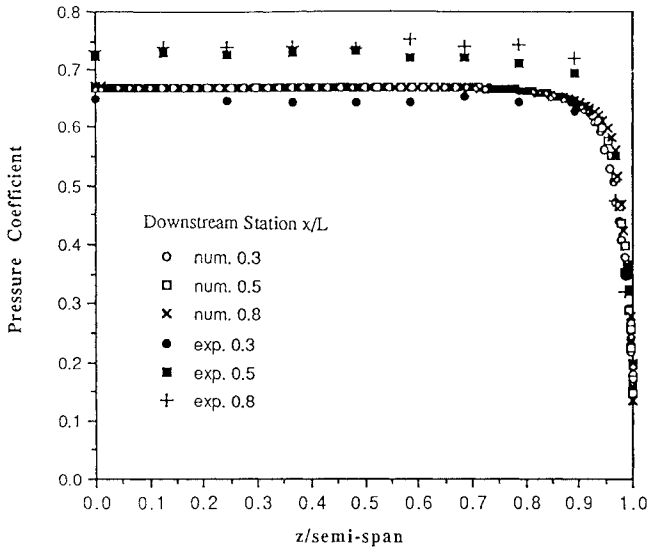

Fig. 16 Comparison of windward pressure coefficient with experiment,[2] present calculation $Re = 2.25 \times 10^6$.

for the general flow features and, in particular, the location of the separation point.

V. Comparison with Experimental Results

Niezgodha et al.[2] have carried out a series of experiments for the delta wing-configuration used in this work in the H2K hypersonic wind tunnel of DLR, Cologne, Germany. Windward pressure measurements were taken at various downstream ports to coincide with the stations used to present the numerical results. No leeward pressure measurements were taken, which is unfortunate as the most interesting flow features occur there. For a freestream Mach number of 8.7 and a freestream Reynolds number of 2.0×10^6/m, the angle of attack was varied between 0 and 30 deg. Figure 16 shows a comparison of pressure measurements with the numerical results of this work for a Reynolds number of 2.25×10^6/m at different downstream stations. The results are in very good agreement close to the nose ($x/L = 0.3$). At stations farther downstream the agreement is within 10%. The accuracy of the pressure measuring system was assessed to be within 2%.

VI. Concluding Remarks

High-resolution calculations have been carried out for a series of inviscid and viscous hypersonic flows over a delta wing at incidence. For the inviscid case, the leeward flow is found to be dominated by a vortex pair produced by shock-induced separation. The resultant pinwheel shock system is found to be similar to that for cone flow under similar freestream conditions and incidence. For the viscous cases, separation is found to occur just inboard of the leading edge. The separation and subsequent vortex formation is found to cause intensive local heating on the leeward surface.

Appendix: Equilibrium Flux Method

The Boltzmann equation is the fundamental equation of the kinetic theory of dilute gases and can be written as

$$\partial(nf)/\partial t + \boldsymbol{c} \cdot \nabla(nf) = \mathcal{D}_c(nf) \qquad \text{(A1)}$$

where n is the number density of the molecules of the gas, $f(\boldsymbol{c}, \varepsilon_{st}, \boldsymbol{r}, t)$ is the molecular velocity distribution function, $\boldsymbol{r}$ is the position, $\boldsymbol{c}$ is the molecular velocity, and ε_{st} is the energy in the molecular structure (i.e., rotational, vibrational, electronic energy, etc.) divided by the mass of the molecule m. The right-hand side (RHS) of Eq. (A1) represents the collision integral. The conservation equations which are solved by EFM can be derived by multiplying Eq. (A1) by the molecular quantities $Q = [m, mc, m((1/2)c^2 + \varepsilon_{st})]$ and integrating over a cell volume V bounded by a surface S, all molecular velocities $\boldsymbol{c}$ and all ε_{st}. The resulting term on the RHS

vanishes. After applying the divergence theorem to the second volume integral on the LHS, we have

$$\frac{\partial}{\partial t}\iiint_V U_Q \, dV + \iint_S F_Q \, dS = 0 \tag{A2}$$

where

$$U_Q = \int_0^\infty \iiint_{-\infty}^{\infty} nQf \, d\mathbf{c} \, d\varepsilon_{st} \tag{A3}$$

and

$$F_Q = \int_0^\infty \iiint_{-\infty}^{\infty} nQf\mathbf{c}\cdot\hat{n} \, d\mathbf{c} \, d\varepsilon_{st} \tag{A4}$$

and where $\iiint_{-\infty}^{\infty} \cdots d\mathbf{c}$ denotes integration over all $\mathbf{c}$. From Eq. (A3) the components of U_Q can be evaluated and, for any nf,

$$U_Q = \left[\rho, \rho\bar{\mathbf{c}}, \rho\left(\tfrac{1}{2}\bar{\mathbf{c}}^2 + e_{int}\right)\right]^T \tag{A5}$$

where

$$\rho = mn, \qquad \bar{\mathbf{c}} = \iiint_{-\infty}^{\infty} f\mathbf{c} \, d\mathbf{c}$$

is the mean molecular velocity or macroscopic fluid velocity and

$$e_{int} = \int_0^\infty \iiint_{-\infty}^{\infty} \left[\frac{1}{2}(\mathbf{c}-\bar{\mathbf{c}})^2 + \varepsilon_{st}\right] f \, d\mathbf{c} \, d\varepsilon_{st}$$

For each cell face, the flux expression can be split into two parts: an outward or forward moving flux F_Q^+ and an inward or backward moving flux F_Q^- where the net flux F_Q is

$$F_Q = F_Q^+ + F_Q^- \tag{A6}$$

In a local coordinate system, the set of forward and backward fluxes are then given by

$$F_Q^+ = \int_{-\infty}^{\infty}\int_{-\infty}^{\infty}\int_0^{\infty} (n^+ f^+) Q c_n dc_n dc_p dc_q \tag{A7}$$

and

$$F_Q^- = \int_{-\infty}^{\infty}\int_{-\infty}^{\infty}\int_{-\infty}^{0} (n^- f^-) Q c_n \, dc_n \, dc_p \, dc_q \tag{A8}$$

where (c_n, c_p, c_q) are the local normal and two tangential components of molecular velocity, respectively. If the form of the distribution functions is known, the transport of mass, momentum, and energy across a cell surface can be calculated analytically. The basis of the equilibrium flux method is the assumption made by Pullin[4] that the gas each side of the surface is in local kinetic equilibrium and, thus, the molecular distribution function is given by Maxwell's equilibrium distribution,

$$f = f_0 = (\beta^3/\pi^{3/2})\exp[-\beta^2(c-\bar{c})^2] \tag{A9}$$

where β is the reciprocal of the most probable thermal speed and is defined by

$$\beta = 1/\sqrt{2RT} \tag{A10}$$

A convenient form of the flux expressions is

$$F_Q^{\pm}\begin{bmatrix} m \\ mc_n \\ mc_p \\ mc_q \\ \frac{1}{2}m\mathbf{c}\cdot\mathbf{c} \end{bmatrix} = \begin{bmatrix} (\rho v_n)^{\pm} W^{\pm} \pm (\rho/\beta)^{\pm} D^{\pm} \\ (\rho v_n v_n + \rho/2\beta^2)^{\pm} W^{\pm} \pm (\rho v_n/\beta)^{\pm} D^{\pm} \\ (\rho v_n v_p)^{\pm} W^{\pm} \pm (\rho v_p/\beta)^{\pm} D^{\pm} \\ (\rho v_n v_q)^{\pm} W^{\pm} \pm (\rho v_q/\beta)^{\pm} D^{\pm} \\ (\rho v_n)^{\pm} W^{\pm}\left\{\dfrac{v^2}{2} + \dfrac{\gamma}{2(\gamma-1)\beta^2}\right\}^{\pm} \pm \left(\dfrac{\rho}{\beta}\right)^{\pm} D^{\pm}\left\{\dfrac{v^2}{2} + \dfrac{1}{4\beta^2}\dfrac{(\gamma+1)}{(\gamma-1)}\right\}^{\pm} \end{bmatrix} \tag{A11}$$

where $v_n = \overline{c_n}$, $v_p = \overline{c_p}$, $v_q = \overline{c_q}$ and $v^2 = v_n^2 + v_p^2 + v_q^2$. The weighting factors W and the dissipation terms D are given by

$$W^{\pm} = \tfrac{1}{2}\left[1 \pm \operatorname{erf}\left(s_n^{\pm}\right)\right] \tag{A12}$$

$$D^{\pm} = \frac{1}{2\sqrt{\pi}}\exp\left\{-\left(s_n^{\pm}\right)^2\right\} \tag{A13}$$

respectively, and s_n is the speed ratio defined as

$$s_n^{\pm} = v_n^{\pm}\beta^{\pm} \tag{A14}$$

These fluxes are expressed in a local coordinate system normal to the cell face under consideration and must be transformed back to a global Cartesian system using a suitable coordinate transformation.

To illustrate how the viscous terms can be combined with the inviscid EFM flux expressions we return to x–y–z coordinates and use the x component of momentum as an example. The flux expression given in Eq. (A6) can be divided into components in the x, y, and z directions to give

$$F_Q(mc_x)A = F_Q(mc_x)_x A_x + F_Q(mc_x)_y A_y + F_Q(mc_x)_z A_z \tag{A15}$$

For the viscous case, these three components can be further divided into the contribution from the inviscid part of the flux and that from the viscous part such that

$$F_Q(mc_x)_x A_x = \{[F_Q(mc_x)_x]_{inv} + [F_Q(mc_x)_x]_{vis}\}A_x \tag{A16}$$

where the subscripts inv and vis refer to the inviscid and viscous components of the flux, respectively. Expansion of the two terms gives

$$F_Q(mc_x)_x A_x = \{F_Q(mc_x)_{inv} n_x - \tau_{xx}\}n_x A \tag{A17}$$

Similar expressions can be derived for the y and z components of Eq. (A15). The resulting expression for the x component of momentum is then

$$F_Q(mc_x)_x A = \{F_Q(mc_x)_{inv} - \tau_{xx}n_x - \tau_{xy}n_y - \tau_{xz}n_z\}A \tag{A18}$$

A similar analysis can be performed on the remaining flux expressions. The changes in mass, momentum, and energy each time step, are then given by

$$\begin{bmatrix} \Delta M \\ \Delta P_x \\ \Delta P_y \\ \Delta P_z \\ \Delta E \end{bmatrix} = \Sigma_{i^{\pm},j^{\pm},k^{\pm}} A\Delta t \times \begin{bmatrix} F_Q(m)_{inv} \\ F_Q(mc_x)_{inv} - \tau_{xx}n_x - \tau_{xy}n_y - \tau_{xz}n_z \\ F_Q(mc_y)_{inv} - \tau_{yx}n_x - \tau_{yy}n_y - \tau_{yz}n_z \\ F_Q(mc_z)_{inv} - \tau_{zx}n_x - \tau_{zy}n_y - \tau_{zz}n_z \\ F_Q(e)_{inv} - n_x\{u\tau_{xx} + v\tau_{xy} + w\tau_{xz} - q_x\} \\ -n_y\{u\tau_{yx} + v\tau_{yy} + w\tau_{yz} - q_y\} \\ -n_z\{u\tau_{zx} + v\tau_{zy} + w\tau_{zz} - q_z\} \end{bmatrix} \tag{A19}$$

where $(u, v, w) = (\overline{c_x}, \overline{c_y}, \overline{c_z})$. If Stokes' hypothesis of zero bulk viscosity is invoked then the nondimensional form of the shear stress and heat transfer terms are

$$\begin{bmatrix} \tau_{xx} \\ \tau_{yy} \\ \tau_{zz} \\ \tau_{xy} \\ \tau_{xz} \\ \tau_{yz} \end{bmatrix} = \begin{bmatrix} \frac{2\tilde{\mu}}{3Re_\infty}\left(2\frac{\partial u}{\partial x} - \frac{\partial v}{\partial y} - \frac{\partial w}{\partial z}\right) \\ \frac{2\tilde{\mu}}{3Re_\infty}\left(2\frac{\partial v}{\partial y} - \frac{\partial w}{\partial z} - \frac{\partial u}{\partial x}\right) \\ \frac{2\tilde{\mu}}{3Re_\infty}\left(2\frac{\partial w}{\partial z} - \frac{\partial u}{\partial x} - \frac{\partial v}{\partial y}\right) \\ \frac{\tilde{\mu}}{Re_\infty}\left(\frac{\partial u}{\partial y} + \frac{\partial v}{\partial x}\right) \\ \frac{\tilde{\mu}}{Re_\infty}\left(\frac{\partial u}{\partial z} + \frac{\partial w}{\partial x}\right) \\ \frac{\tilde{\mu}}{Re_\infty}\left(\frac{\partial v}{\partial z} + \frac{\partial w}{\partial y}\right) \end{bmatrix} \tag{A20}$$

$$\begin{bmatrix} q_x \\ q_y \\ q_z \end{bmatrix} = -\frac{\tilde{\mu}}{(\gamma - 1)M_\infty^2 Re_\infty Pr} \begin{bmatrix} \frac{\partial T}{\partial x} \\ \frac{\partial T}{\partial y} \\ \frac{\partial T}{\partial z} \end{bmatrix} \tag{A21}$$

In Eqs. (A20) and (A21) all quantitities are made dimensionless with respect to freestream conditions and body length L, $\tilde{\mu} = \mu(T)/\mu(T_\infty)$ and $Pr = \mu(T)C_p/\kappa(T)$ where C_p is the constant-pressure specific heat and $\kappa(T)$ is the coefficient of heat conductivity.

Acknowledgments

This work was partially supported by the Australian Research Council under Grant A89031403 and by the AFOSR under Grant F49620-93-1-0338. E. R. Mallett acknowledges the award of a Walter and Eliza Hall Travelling Scholarship. The authors wish to acknowledge the help and advice given by members of the Caltech Concurrent Supercomputing Facility (CCSF).

References

[1]Whitehead, A. H., Jr., "Effect of Vortices on Delta Wing Leeward Flow at Mach 6," *AIAA Journal*, Vol. 8, No. 3, 1970, pp. 599, 600.

[2]Niezgodha, J., Henckels, A., and Weiland, C., "Pressure Measurements and Infrared Observation on the Windward side of a Delta Wing," *Hypersonic Flows for Reentry Problems*, edited by R. Abrall et al., Springer–Verlag, New York, 1992.

[3]Marconi, F., "Complex Shock Patterns and Vortices in Inviscid Supersonic Flows," *Computers and Fluids*, Vol. 17, No. 1, 1989, pp. 151–163.

[4]Pullin, D. I., "Direct Simulation Methods for Compressible Inviscid Ideal-Gas Flow," *Journal of Computational Physics*, Vol. 34, No. 2, 1980, pp. 231–244.

[5]Macrossan, M. N., Mallett, E. R., and Pullin, D. I., "Flow Calculations for the Hermes Delta-Wing with a Second-Order Kinetic-Theory Based on Euler Solver," Workshop on Hypersonic Flow for Reentry Problems, Pt. 2 (Antibes, France), April 1991 (Paper C4).

[6]Macrossan, M. N., "The Equilibrium Flux Method for the Calculation of Flows with Nonequilibrium Chemical Reactions," *Journals of Computational Physics*, Vol. 80, No. 1, 1989, pp. 204–231.

[7]Macrossan, M. N., "Hypervelocity Flow of Dissociating Nitrogen Downstream of a Blunt Nose," *Journal of Fluid Mechanics*, Vol. 217, 1990, pp. 167–202.

[8]Macrossan, M. N., and Pullin, D. I., "A Computational Investigation of Inviscid Hypervelocity Dissociating Flow Past a Cone of Incidence," *Journal of Fluid Mechanics*, Vol. 226, 1994, pp. 69–92.

[9]Anderson, W. K., Thomas, J. L., and van Leer, B., "A Comparison of Finite Volume Flux Vector Splittings for the Euler Equations," AIAA Paper 85-0122, 1985.

[10]Flynn, M. J., "Very High Speed Computing Systems," *Proceedings of the IEEE*, Vol. 54, No. 12, 1966, pp. 1901–1909.

[11]Mallett, E. R., "A Numerical Study of Hypersonic Leeward Flow over the Delta-Wing of the Hermes Spacecraft Using a Parallel Architecture Supercomputer," Ph.D. Thesis, Dept. of Mechanical Engineering, Univ. of Queensland, Australia, 1993.

[12]Anon., *Express Users Guide*, Parasoft, Pasadena, CA, 1992.

[13]Hornung, H., and Perry, A. E., "Some Aspects of Three-Dimensional Separation, Part 1: Stream-Surface Bifurcations," *Zeitschrift für Flugwissenschaften Weltraumforschung*, Vol. 8, 1984, pp. 77–87.

[14]LeToullec, L., and Guillen, P., "Hypersonic Delta-Wing Flow Calculations Using a Multi-Domain MUSCL Euler Solver," *Proceedings of the Workshop on Hypersonic Flows for Re-entry Problems* (Antibes, France), Institut National de Recherche en Informatique et en Automatique, Antibes, France, 1991, pp. 1–19.

[15]Menne, S., "Contribution to HERMES Antibes Workshop," *Proceedings of the Workshop on Hypersonic Flows for Re-entry Problems* (Antibes, France), Institut National de Recherche en Informatique et en Automatique, Antibes, France, 1991, pp. 39–84.